

Mid-ocean ridge unfauling revealed by magmatic intrusions

<https://doi.org/10.1038/s41586-024-07247-w>

Received: 23 June 2023

Accepted: 27 February 2024

Published online: 10 April 2024

 Check for updates

Jean-Arthur Olive^{1✉}, Göran Ekström², W. Roger Buck², Zhonglan Liu³, Javier Escartín¹ & Manon Bickert⁴

Mid-ocean ridges (MORs) are quintessential sites of tectonic extension^{1–4}, at which divergence between lithospheric plates shapes abyssal hills that cover about two-thirds of the Earth's surface^{5,6}. Here we show that tectonic extension at the ridge axis can be partially undone by tectonic shortening across the ridge flanks. This process is evidenced by recent sequences of reverse-faulting earthquakes about 15 km off-axis at the Mid-Atlantic Ridge and Carlsberg Ridge. Using mechanical models, we show that shallow compression of the ridge flanks up to the brittle failure point is a natural consequence of lithosphere unbending away from the axial relief. Intrusion of magma-filled fractures, which manifests as migrating swarms of extensional seismicity along the ridge axis, can provide the small increment of compressive stress that triggers reverse-faulting earthquakes. Through bathymetric analyses, we further find that reverse reactivation of MOR normal faults is a widely occurring process that can reduce the amplitude of abyssal hills by as much as 50%, shortly after they form at the ridge axis. This 'unfauling' mechanism exerts a first-order influence on the fabric of the global ocean floor and provides a physical explanation for reverse-faulting earthquakes in an extensional environment.

Normal faults are key contributors to the seismic activity of MORs^{1–4}. Over hundreds of thousands of years, these faults offset and tilt newly accreted volcanic seafloor, shaping regularly spaced abyssal hills^{5–7}. Notably, normal faults with the largest offsets are typically found on the edges of axial valleys, but almost never in the outer ridge flanks (Fig. 1). This observation, made in the 1970s before multibeam bathymetric data became widely available, led several authors to formulate the concept of abyssal-hill unfauling, that is, the notion that MOR normal faults experience reverse slip that shortens their offsets as they migrate up the ridge flanks^{8–11}. This idea lost favour because no clear driving mechanism had been identified and, most importantly, because reverse-faulting earthquakes compatible with ridge-normal compression near the axis had not been reported¹². Reverse-faulting events are well documented hundreds of kilometres from MOR axes¹³, in oceanic lithosphere older than 10–20 Myr, in which a compressive stress state is expected¹⁴. Rare reverse-faulting events have also been observed in lithosphere as young as 3 Myr (about 30 km from the axis at slow spreading rates¹³) or even closer to the axis in the vicinity of transform faults¹⁵. Surprisingly, these events indicate both ridge-parallel and ridge-normal compression (Extended Data Fig. 1a) and have been attributed to thermal stresses¹⁶, the complex stress state of ridge-transform intersections¹⁷ or recent shifts in plate motion¹⁸. Clear manifestations of near-axis (<30 km) compressive seismicity have, overall, remained elusive, until late 2022.

Swarms of reverse-faulting earthquakes

On 26 September 2022, a particularly active swarm of earthquakes with moment magnitudes $M_w > 4$ began at 54° N on the northern Mid-Atlantic

Ridge^{19,20} (Fig. 1a). This slow-spreading segment (2.2 cm year⁻¹ of full plate-separation rate) is located north of the Charlie-Gibbs Fracture Zone and bounded by two non-transform offsets. Its symmetric morphology is typical of a magmatically robust ridge section (in the sense of ref. 21), with an approximately 1.3 km deep axial valley flanked by two shoulders and abyssal-hill-bounding normal faults with a characteristic spacing of 2–4 km (Fig. 1c). During the first three days of the 2022 swarm, relocated seismicity (Methods; Supplementary Table 1) showed southward migration along the axial valley by roughly 45 km (Extended Data Fig. 2a) and entirely consisted of E–W extensional mechanisms. This normal-faulting activity continued for 27 more days without clear signs of further migration. 80 h into the swarm, a magnitude-5.1 reverse-faulting earthquake indicative of ridge-normal compression occurred below the summit of the ridge shoulder, 15 km east of the neovolcanic axis. Between 29 September 2022 and 4 January 2023, 11 more reverse-faulting events with M_w up to 5.9 occurred on N–S striking, approximately 45–50°-dipping planes, outlining two narrow bands symmetrically located about 15 km east and west of the ridge axis (Fig. 1a). Inspection of the teleseismic P waveforms from the largest compressive events shows a very short delay between the direct P arrival and phases reflected off the seafloor and sea surface. This implies remarkably shallow hypocentre depths, which we estimate within 2–5 km below the seafloor (Methods).

We identified a similar pattern in a November 2014 earthquake sequence on the slow-spreading Carlsberg Ridge at 6° N in the Indian Ocean (full spreading rate: 2.4 cm year⁻¹; Fig. 1b,d). There, a less active swarm of $M_w \approx 5$ normal-faulting seismicity at the ridge axis (with possible, although unclear, southeastward migration; Extended Data

¹Laboratoire de Géologie, CNRS - École Normale Supérieure - PSL University, Paris, France. ²Lamont-Doherty Earth Observatory, Columbia University, Palisades, NY, USA. ³College of Earth Sciences, Jilin University, Changchun, China. ⁴Geo-Ocean, Univ. Brest, CNRS, Ifremer, UMR6538, Plouzané, France. ✉e-mail: olive@geologie.ens.fr

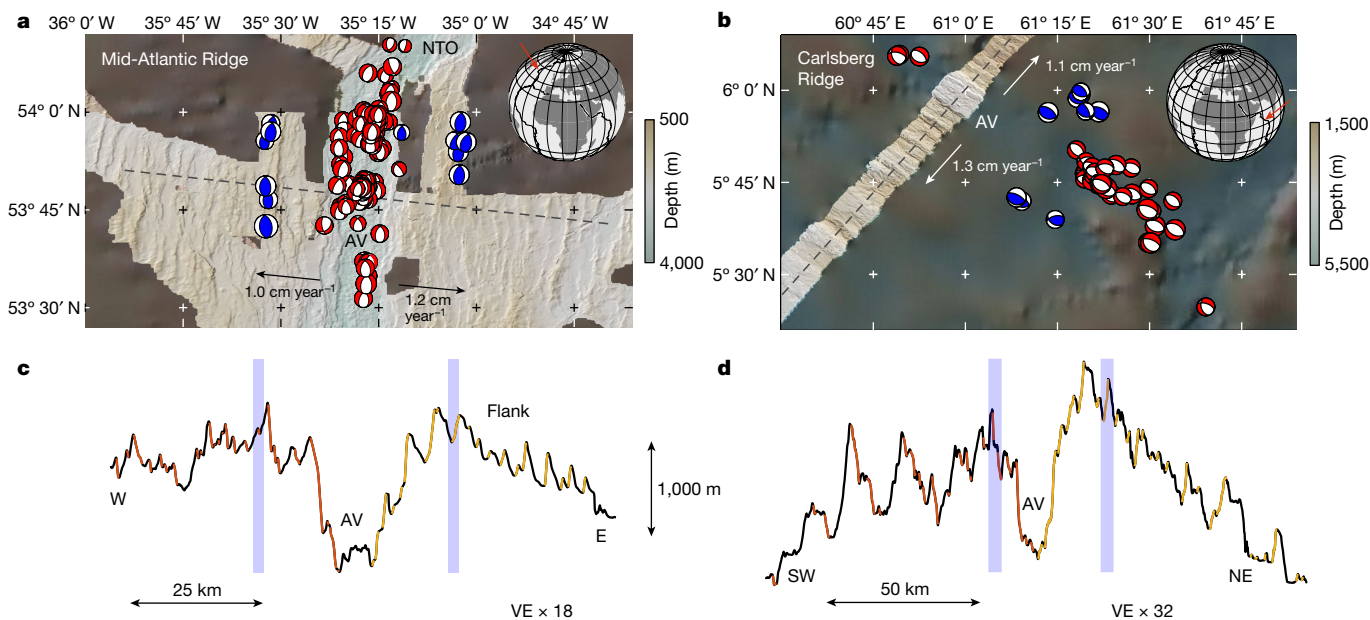


Fig. 1 | Swarms of normal and reverse seismicity at two slow-spreading MORs. **a**, Bathymetry of the 54° N segment of the northern Mid-Atlantic Ridge⁵⁰, showing relocated earthquakes from the 2022 swarm. Red and blue beach balls show normal and reverse mechanisms, respectively. **b**, Bathymetry of the Carlsberg Ridge near 6° N, with relocated 1990–2020 seismicity (Global CMT catalogue³⁵). Shading shows zones with multibeam data (visible fault

scarps) versus interpolated bathymetry (textureless). **c**, Topographic cross-section along the dashed line in panel **a**, with fault scarps shown in red (west side) and yellow (east side). Blue bars indicate the projected location of reverse-faulting events. **d**, Topographic cross-section along the dashed line in panel **b**: closest available transect with shipboard bathymetry. AV, axial valley; NTO, non-transform offset; VE, vertical exaggeration.

Fig. 2e–h) preceded five reverse-faulting events about 15 km northeast and southwest of the ridge axis. Notably, both ridge flanks had produced similar $M_w \approx 5$ –5.3 reverse-faulting events in 2005 and 2009 that were not preceded by a detectable swarm of normal-faulting earthquakes.

Compression of MOR flanks

Sparse bathymetric data show that the 6° N segment of the Carlsberg Ridge is morphologically similar to the 54° N segment of the Mid-Atlantic Ridge, with even more pronounced axial relief (Fig. 1c,d). By summing the offsets of large normal faults on both sides of the axis^{22–24} (Methods), we estimate the tectonically accommodated fraction of plate separation T at about 15% in both segments (Fig. 2). The remaining

85% of plate divergence occurs through magmatic emplacement and could be achieved by, for example, the intrusion of a metre-wide dyke through the axial lithosphere roughly every 50 years (refs. 25,26). Such partitioning of magmatic and tectonic strain probably explains the formation of regularly spaced abyssal hills bounded by faults that accumulate normal offsets as large as approximately 500 m when they grow along the edges of the axial valley^{7,27,28}. The geometry of the compressive events detected in both segments, however, indicates that the shallow portion of these normal faults can be reactivated in a reverse sense once they migrate out of the axial valley and reach the top of the ridge shoulders.

Standard numerical simulations of MORs show that the formation of an axial valley results in compressional faulting on the ridge

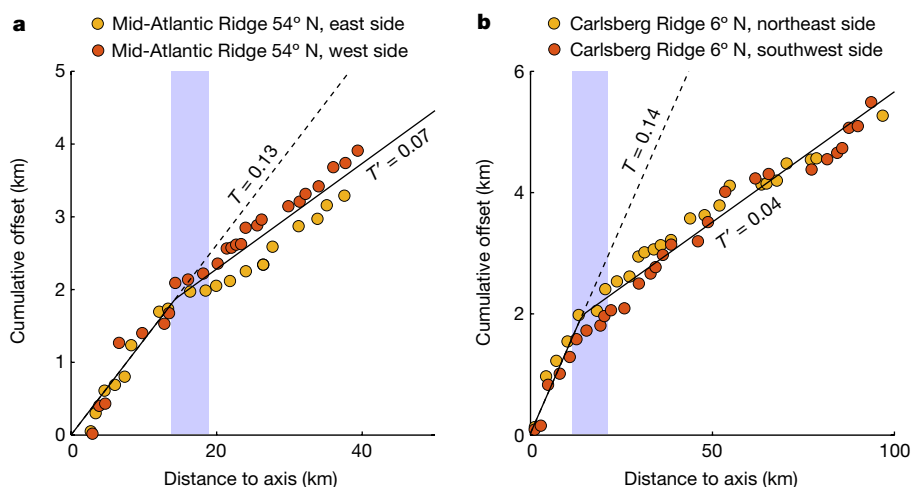


Fig. 2 | Tectonic strain and the bathymetric signature of unfauling. Plots of cumulative fault heave versus distance from the axis for the Mid-Atlantic Ridge at 54° N (**a**) and the Carlsberg Ridge at 6° N (**b**). Blue bands mark the location of

reverse-faulting events. Black lines show best-fitting piecewise linear function, with slope T (the tectonic fraction of plate separation) near the ridge axis and slope T' further off-axis.

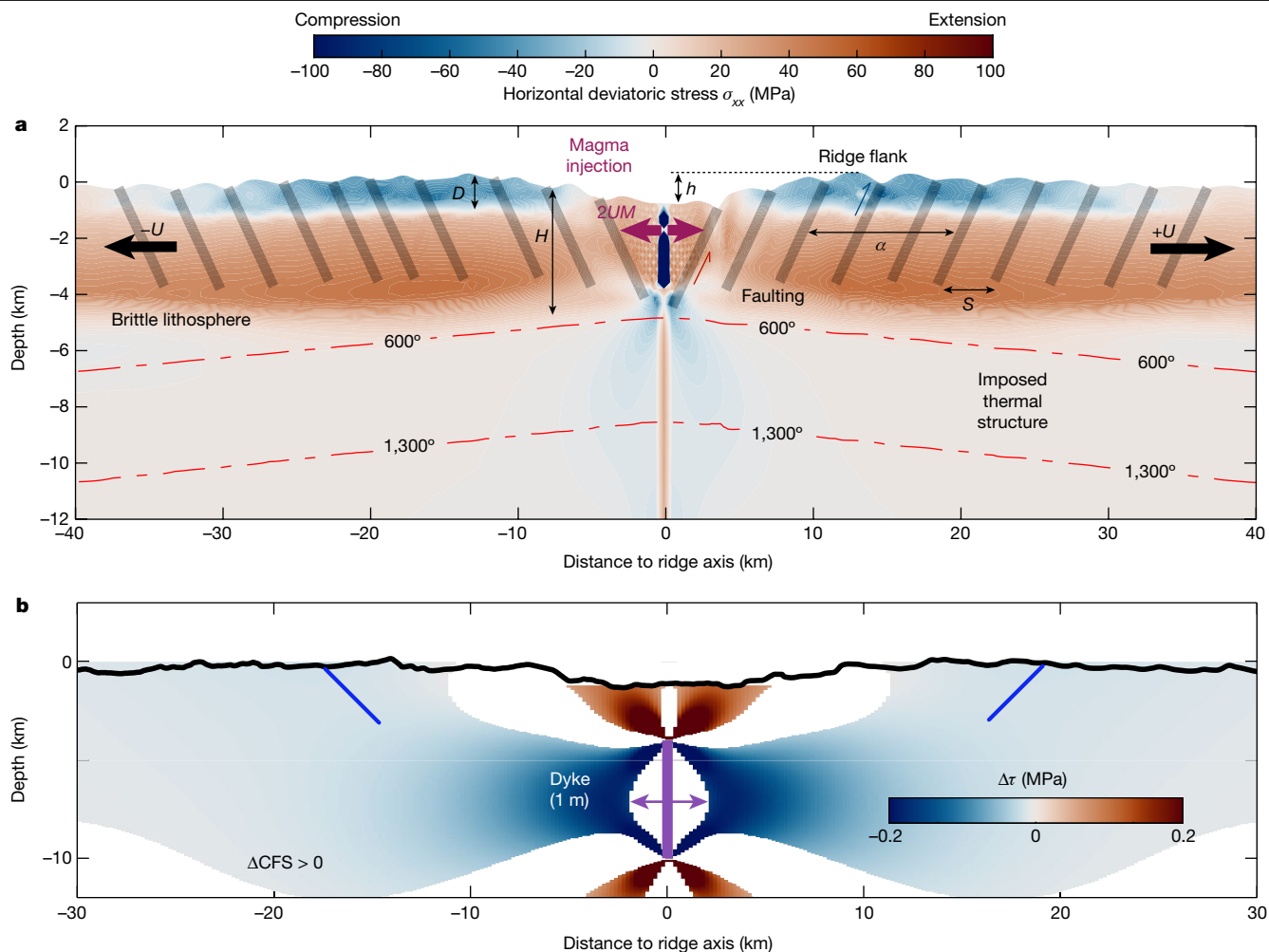


Fig. 3 | The stress state of MOR shoulders. **a**, Cross-section of the horizontal deviatoric stress in a 2D numerical model of seafloor spreading developing an axial valley and symmetric shoulders^{30,31}. See text for meaning of symbols. **b**, Change in shear stress ($\Delta\tau$) resolved on 45°-dipping faults (>0 and <0 indicates

normal and reverse motion, respectively) induced by 1 m of dyke opening (purple line), shown only in areas in which the Coulomb stress change (ΔCFS) brings faults closer to failure. Black line shows relief of the 54° segment of the Mid-Atlantic Ridge.

flanks, even when dyke intrusion accounts for most of the plate spreading (Fig. 3a). Here we model an idealized 2D cross-axis section of a slow-spreading centre in which a fraction $M (= 1 - T)$ of the far-field extension ($2U$) is accommodated by continuous magmatic emplacement in a narrow axial zone^{27–29}. In this simulation, the value of M is a self-evolving function of the axial relief, which accounts for mechanical feedbacks between relief development and dyke intrusions in the axial zone^{30,31} (Methods). M is adjusted to yield a characteristic abyssal-hill spacing of approximately 3 km following ref. 7. The development of shoulders is a natural consequence of the vertical displacement that accompanies tectonic extension at the ridge axis: as it moves off-axis, uplifted lithosphere must unbend to transition to a state of rigid horizontal motion³². This occurs over a characteristic flexural length scale α modulated by the integrated strength of young oceanic lithosphere. In the simulation shown in Fig. 3a, the thermal structure of the ridge is fixed and chosen such that the visco-elasto-plastic lithosphere flexes into shoulders similar to those of the 54° N segment of the Mid-Atlantic Ridge. This produces a zone of shallow horizontal compression about 25 km wide and about 2 km deep, beginning 6 km from the magma injection zone on both ridge flanks (Fig. 3a). The associated horizontal deviatoric stresses exceed tens of MPa and reach the point of compressive Mohr–Coulomb failure, with stresses that peak roughly 15 km off-axis. This stress field is consistent with the occurrence of shallow, ridge-perpendicular,

reverse-faulting earthquakes near the summit of the ridge flanks (Fig. 1c,d).

The shallow compressive strain produced by unbending of the ridge flanks can be estimated through an order-of-magnitude approach as the ratio of the compressive zone thickness D (about 2 km in Fig. 3a) to the radius of curvature of the lithosphere³³. A simple unbending model^{20,34} relates the radius of curvature to the amplitude h of the axial relief (about 1.5 km) and the flexural length scale α (about 10 km). This gives a strain $\epsilon \approx Dh/\alpha^2$ on the order of 0.03, large enough to leave a detectable signature in seafloor relief.

The bathymetric signature of unroofing

At both the northern Mid-Atlantic Ridge and the Carlsberg Ridge, we detect a sharp break in the trend of cumulative fault offset versus off-axis distance, at about 15 km, roughly co-located with the bands of compressive earthquakes (Fig. 2). The break in slope corresponds to a reduction in the apparent fraction T of tectonic extension by 0.06–0.10. We interpret this break in slope as a reduction of the average offset on abyssal-hill-bounding faults caused by cumulative reverse slip (Fig. 4a). To the first order, T corresponds to the characteristic normal-fault heave (the horizontal component of fault offset) divided by the characteristic fault spacing. Therefore, a decrease from $T = 0.13$ to $T = 0.07$ (Fig. 2a) can represent a reduction in heave from about 400 m down to

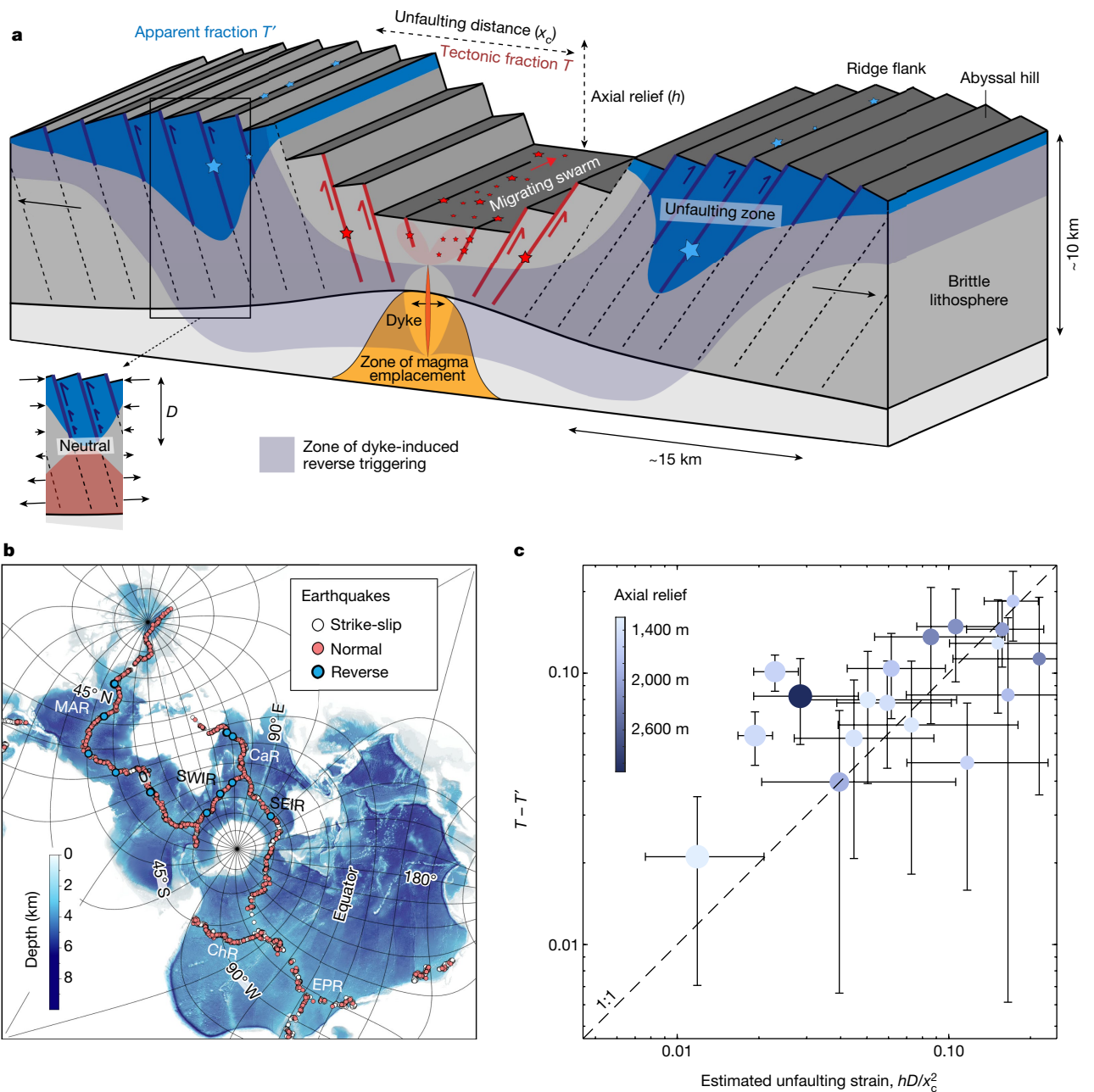


Fig. 4 | MOR unfauling. a, Illustration showing the shallow flexural compression of MOR flanks and the occasional triggering of reverse slip by a magmatic intrusion. Red and blue stars represent extensional and reverse-faulting earthquakes, respectively. Inset illustrates the depth-dependent stress state of unbending lithosphere, with shallow compression (blue) and deep extension (red). **b**, Spilhaus projection map of MOR strike-slip and normal-faulting earthquakes from the Global CMT catalogue. Blue dots show reverse-faulting earthquakes that occurred in areas with a documented signature of bathymetric unfauling (see Supplementary Information). **c**, Relationship between the

change in apparent T fraction ($T - T'$) and unfauling strain (ϵ), estimated as the product of axial relief (h) by the depth of the unfauling zone (D , here assumed to equal 5 km everywhere) divided by the unfauling distance x_c (here used as a proxy for flexural wavelength α) squared. Error bars (95% confidence bounds) are derived from the nonlinear least-squares fit to the cumulative offset plots (for example, Fig. 2; see Methods). Size of the symbols scales with x_c . CaR, Carlsberg Ridge; ChR, Chile Ridge; EPR, East Pacific Rise; MAR, Mid-Atlantic Ridge; SEIR, Southeast Indian Ridge; SWIR, Southwest Indian Ridge.

about 200 m for a population of faults evenly spaced by approximately 3 km, a scenario consistent with the morphology of the 54° N segment of the Mid-Atlantic Ridge (Fig. 1c).

The Carlsberg Ridge and the northern Mid-Atlantic Ridge are not unique in hosting near-axis reverse-faulting earthquakes. More than a dozen comparable events can be found throughout the Global Centroid Moment Tensor (CMT) catalogue^{20,35}, along the ultraslow-spreading Southwest Indian Ridge, the slow-spreading Mid-Atlantic Ridge and Carlsberg Ridge, as well as the intermediate-spreading

Southeast Indian Ridge (Extended Data Figs. 1 and 3). On the basis of low-resolution bathymetric and gravity data, ref. 20 attributed these events to unbending in the footwall of large-offset detachment faults, at which small-magnitude reverse seismicity had previously been documented³⁶. This interpretation is, however, at odds with available high-resolution bathymetry data: out of the 13 ridge sections that have hosted reverse-faulting earthquakes and have been mapped with shipboard multibeam echosounders (Fig. 4b and Supplementary Tables 2 and 3), ten show a magmatically robust morphology (in the

sense of ref. 21) with symmetric, staircase-like abyssal hills bounded by short-offset faults (Extended Data Figs. 1 and 3). Although the other three do host scattered detachment faults, a systematic co-location with the reverse quakes is difficult to establish given the large location uncertainties of teleseismic events. Analysing representative bathymetric profiles from all of these ridge sections systematically yields a reduction in the apparent T fraction by 0.02–0.18 at distances ranging from about 10 to 30 km off-axis (Extended Data Figs. 1, 4 and 5). Also, revisiting a published database of 2,157 normal faults identified along the intermediate-spreading Chile Ridge²⁴—for which we found no near-axis compressive event in the CMT catalogue—yields a similar pattern at the scale of the entire ridge (Extended Data Figs. 6–8 and Supplementary Tables 3 and 4). There, $T - T' \approx 0.07$, but the shift occurs slightly closer to the ridge axis, within about 7–16 km from the neovolcanic zone.

It is important to note that processes other than unroofing could contribute to a reduction in apparent T fraction across the flanks of magmatically robust ridge sections. These include sedimentation filling bathymetric lows and reducing the apparent amplitude of abyssal hills. Median sediment thickness, however, only increases by about 5 m per Myr of seafloor age^{37–40}. Sedimentary infilling is thus unlikely to account for more than about 30 m of apparent offset reduction (for example, $T - T' < 10^{-2}$) in areas of suspected unroofing. On the other hand, gravitational mass wasting is known to alter the slopes of axis-facing fault scarps by maintaining them at or below the frictional angle of repose (approximately 35°) through repeated rock sliding^{41,42}. The progressive nature of this process, however, seems at odds with the abruptness of the reduction in apparent T fraction (Fig. 2), unless the reduction marks the point at which normal slip on abyssal hill faults ceases and mass wasting begins to overcome tectonic uplift. We do not favour this endmember interpretation because fault scarps seem to migrate across the unroofing zone without any detectable change in their average slope (Extended Data Fig. 6d). Furthermore, axis-facing scarps on the fast-spreading East Pacific Rise—which presumably experience gravitational mass wasting like other ridge sections—show an increase in apparent T fraction about 17 km off-axis (Extended Data Fig. 9). This increase is readily explained by unbending away from an axial high³⁴ ($T - T' < 0$), mirroring the unbending away from an axial valley ($T - T' > 0$; Fig. 4a). We conclude that changes in apparent T fraction primarily reflect shallow flexural strains reworking the tectonic fabric of abyssal hills, as opposed to surface processes.

Available bathymetric data suggest that the unroofing process as summarized in Fig. 4a primarily occurs at magmatically robust ($T \leq 0.2$) MOR sections with an axial valley flanked by pronounced ridge shoulders. It does not rule out the occurrence of unbending quakes in the footwall of oceanic detachments as proposed by ref. 20, but the impact of such events on ocean-floor physiography is not as clear. As a measure of normal-fault shortening, $T - T'$ provides a proxy for the horizontal strain associated with shoulder compression. Its typical value (approximately 0.07), however, exceeds our initial order-of-magnitude estimate of $\varepsilon \approx 0.03$. One reason could be that the depth extent of reverse slip is greater than predicted by our numerical models (Fig. 3a), for example, $\varepsilon \approx 0.07$ if D extends to about 5 km instead of about 2 km below the seafloor, consistent with the depths of near-axis reverse-faulting earthquakes²⁰ (Supplementary Table 1). This could be achieved if the effective frictional strength of the shallow, compressed lithosphere was reduced, for example, by the pressurization of pore fluids trapped in abyssal-hill-bounding faults. Supra-hydrostatic pore pressures could plausibly deepen the neutral bending plane in MOR shoulders down to about 5 km or deeper (Extended Data Fig. 10) and would also have the effect of narrowing the cross-axis extent of the unroofing zone, contributing to a more abrupt decrease in apparent T (see Supplementary Information). Further, assuming $D = 5$ km and using the unroofing distance (the position

x_c of the sudden decrease in T) as a proxy for the flexural wavelength a to estimate the unroofing strain ε yields a reasonable agreement with our measurements of $T - T'$ across all candidate unroofing sites (Fig. 4c).

Role of magmatic intrusions

The widespread bathymetric signature of abyssal-hill unroofing contrasts with its relative scarcity in the seismic record (Fig. 4b). The moment rate associated with extensional faulting at the axis straightforwardly scales as $\dot{M}_E \approx G U H_0$ (per unit length along the ridge axis, with G the shear modulus and H_0 the thickness of the axial lithosphere; ref. 43). The seafloor-shortening rate in the ridge flanks can be estimated as the spreading half-rate times the reduction in fault heave per unit distance away from the axis, that is, $\varepsilon U = (T - T')U$. Along the neutral plane located at depth D (Figs. 3a and 4a), there is no shortening. Consequently, the shortening rate averaged over the thickness of the compressive domain is $(T - T')U/2$. It follows that the moment rate associated with reverse slip should scale as $\dot{M}_R \approx G U (T - T')D/2$, and $\dot{M}_R/\dot{M}_E \approx \frac{(T - T')D}{2H_0}$. Assuming $D = H_0 \approx 5$ km, $T - T' \approx 0.07$ and $T \approx 0.15$ yields $\dot{M}_R/\dot{M}_E \approx 0.2$. Reference 20 estimated the total moment rate of near-axis reverse-faulting events in the CMT catalogue as the equivalent of 1.5 $M_w 5.5$ earthquakes per year for the period 1985–2023, which is about 5% of the moment rate associated with normal-faulting events ($\dot{M}_R/\dot{M}_E \approx 0.05$). One explanation for this discrepancy could be that reverse slip in the shallow ridge flanks is more aseismic than normal slip on the edge of the axial valley. This would be consistent with supra-hydrostatic pore-fluid pressures in the unroofing zone, which increase the characteristic nucleation size of earthquakes and favour a regime in which aseismic reverse-slip transients account for greater cumulative displacements than reverse-faulting earthquakes^{43–45}.

The idea that flexural stresses alone cause reverse-faulting earthquakes only sporadically is consistent with the fact that the two clearest manifestations of the unroofing process, the 2014 Carlsberg Ridge and the 2022 Mid-Atlantic Ridge swarms, were plausibly triggered by a dyke-intrusion event¹⁹. In both instances, the reverse-faulting earthquakes were preceded by on-axis swarms of extensional seismicity, with a pattern of southward migration at about 0.2 m s⁻¹ in the Atlantic case. Migrating seismicity at rates of approximately 0.1–1.0 m s⁻¹ has unambiguously been linked to dyke propagation in Iceland and Ethiopia^{46,47}, and similar swarms have been observed at magmatically active segments of the Juan de Fuca Ridge⁴⁸ and the Gakkel Ridge⁴⁹. It is thus likely that the initial swarm of extensional earthquakes was the manifestation of a magmatic fissure propagating along the ridge axis. Standard elastic dislocation modelling (Fig. 3b; Methods) shows that opening of a vertical dyke between 4 and 10 km below the axial valley floor induces static Coulomb stress changes that promote normal slip on axial valley faults while promoting shallow reverse slip roughly 15 km off-axis. Magmatic fissures are typically about 1 m wide at oceanic spreading centres²⁵. A dyke intrusion such as those inferred at the Carlsberg Ridge and the Mid-Atlantic Ridge may thus represent a one-in-50-year event that precipitated the occurrence of otherwise elusive unroofing earthquakes (Fig. 4a). Although not necessary to drive reverse slip on MOR normal faults, magmatic intrusions may have been instrumental in revealing this fundamental component of seafloor spreading, which—over geological time—strongly reworks the fabric of the global ocean floor.

Online content

Any methods, additional references, Nature Portfolio reporting summaries, source data, extended data, supplementary information, acknowledgements, peer review information; details of author contributions and competing interests; and statements of data and code availability are available at <https://doi.org/10.1038/s41586-024-07247-w>.

1. Sykes, L. R. Mechanism of earthquakes and nature of faulting on the mid-oceanic ridges. *J. Geophys. Res.* **72**, 2131–2153 (1967).
2. Engeln, J. F., Wiens, D. A. & Stein, S. Mechanisms and depths of Atlantic transform earthquakes. *J. Geophys. Res.* **91**, 548–577 (1986).
3. Huang, P. Y., Solomon, S. C., Bergman, E. A. & Nabelek, J. L. Focal depths and mechanism of Mid-Atlantic Ridge earthquakes from body waveform inversion. *J. Geophys. Res.* **91**, 579–598 (1986).
4. Solomon, S. C., Huang, P. Y. & Meinke, L. The seismic moment budget of slowly spreading ridges. *Nature* **334**, 58–60 (1988).
5. Menard, H. W. & Mammerickx, J. Abyssal hills, magnetic anomalies and the East Pacific Rise. *Earth Planet. Sci. Lett.* **2**, 465–472 (1967).
6. Macdonald, K. C., Fox, P. J., Alexander, R. T., Pockalny, R. & Gente, P. Volcanic growth faults and the origin of Pacific abyssal hills. *Nature* **380**, 125–129 (1996).
7. Olive, J.-A. et al. Sensitivity of seafloor bathymetry to climate-driven fluctuations in mid-ocean ridge magma supply. *Science* **350**, 310–313 (2015).
8. Deffeyes, K. S. in *Megatectonics of Continents and Oceans* (eds Johnson, J. & Smith, B. L.) 194–222 (Rutgers Univ. Press, 1970).
9. Osmaston, M. F. Genesis of ocean ridge median valleys and continental rift valleys. *Tectonophysics* **11**, 387–405 (1971).
10. Harrison, C. G. A. Tectonics of mid-ocean ridges. *Tectonophysics* **22**, 301–310 (1974).
11. Macdonald, K. C. Mid-ocean ridges: fine scale tectonic, volcanic and hydrothermal processes within the plate boundary zone. *Annu. Rev. Earth Planet. Sci.* **10**, 155–190 (1982).
12. Needham, H. D. & Francheteau, J. Some characteristics of the Rift Valley in the Atlantic Ocean near 36° 48' north. *Earth Planet. Sci. Lett.* **22**, 29–43 (1974).
13. Bergman, E. A. & Solomon, S. C. Source mechanisms of earthquakes near mid-ocean ridges from body waveform inversion: implications for the early evolution of oceanic lithosphere. *J. Geophys. Res.* **89**, 11415–11441 (1984).
14. Fleitout, L. & Froidevaux, C. Tectonic stresses in the lithosphere. *Tectonics* **2**, 315–324 (1983).
15. Wolfe, C. J., Bergman, E. A. & Solomon, S. C. Oceanic transform earthquakes with unusual mechanisms or locations: relation to fault geometry and state of stress in the adjacent lithosphere. *J. Geophys. Res.* **98**, 16187–16211 (1993).
16. Turcotte, D. L. Are transform faults thermal contraction cracks? *J. Geophys. Res.* **79**, 2573–2577 (1974).
17. Behn, M. D., Lin, J. & Zuber, M. T. Evidence for weak oceanic transform faults. *Geophys. Res. Lett.* **29**, 2207 (2002).
18. Janin, A. et al. Tectonic evolution of a sedimented oceanic transform fault: the Owen Transform Fault, Indian Ocean. *Tectonics* **42**, e2023TC007747 (2023).
19. Cesca, S., Metz, M., Büyükkapınar, P. & Dahm, T. The energetic 2022 seismic unrest related to magma intrusion at the North Mid-Atlantic Ridge. *Geophys. Res. Lett.* **50**, e2023GL102782 (2023).
20. Jackson, J. & McKenzie, D. Reverse-faulting earthquakes and the tectonics of slowly-spreading mid-ocean ridge axes. *Earth Planet. Sci. Lett.* **618**, 118279 (2023).
21. Escartin, J. et al. Central role of detachment faults in accretion of slow-spreading oceanic lithosphere. *Nature* **455**, 790–794 (2008).
22. Searle, R. C. & Laughton, A. S. Sonar studies of the Mid-Atlantic Ridge and Kurchatov Fracture Zone. *J. Geophys. Res.* **82**, 5313–5328 (1977).
23. Escartin, J. et al. Quantifying tectonic strain and magmatic accretion at a slow spreading ridge segment, Mid-Atlantic Ridge, 29°N. *J. Geophys. Res.* **104**, 10421–10437 (1999).
24. Howell, S. et al. Magmatic and tectonic extension at the Chile Ridge: evidence for mantle controls on ridge segmentation. *Geochem. Geophys. Geosyst.* **17**, 2354–2373 (2016).
25. Qin, R. & Buck, W. R. Why meter-wide dikes at spreading centers? *Earth Planet. Sci. Lett.* **265**, 466–474 (2008).
26. Olive, J.-A. & Dublanche, P. Controls on the magmatic fraction of extension at mid-ocean ridges. *Earth Planet. Sci. Lett.* **549**, 116541 (2020).
27. Buck, W. R., Lavier, L. L. & Poliakov, A. N. B. Modes of faulting at mid-ocean ridges. *Nature* **434**, 719–723 (2005).
28. Behn, M. D. & Ito, G. Magmatic and tectonic extension at mid-ocean ridges: 1. Controls on fault characteristics. *Geochem. Geophys. Geosyst.* **9**, Q08O10 (2008).
29. Tucholke, B. E. et al. Role of melt supply in oceanic detachment faulting and formation of megamullions. *Geology* **36**, 455–458 (2008).
30. Liu, Z. & Buck, W. R. Global trends of axial relief and faulting at plate spreading centers imply discrete magmatic events. *J. Geophys. Res.* **125**, e2020JB019465 (2020).
31. Liu, Z. & Buck, W. R. Magmatic controls on axial relief and faulting at mid-ocean ridges. *Earth Planet. Sci. Lett.* **491**, 226–237 (2018).
32. Qin, R. & Buck, W. R. Effect of lithospheric geometry on rift valley relief. *J. Geophys. Res.* **110**, B03404 (2005).
33. Turcotte, D. L. & Schubert, G. *Geodynamics* 2nd edn (Cambridge Univ. Press, 2002).
34. Buck, W. R. Accretional curvature of lithosphere at magmatic spreading centers and the flexural support of axial highs. *J. Geophys. Res.* **106**, 3953–3960 (2001).
35. Ekström, G., Nettles, M. & Dziewonski, A. M. The global CMT project 2004–2010: centroid-moment tensors for 13,017 earthquakes. *Phys. Earth Planet. Inter.* **200–201**, 1–9 (2012).
36. Parnell-Turner, R. et al. Oceanic detachment faults generate compression in extension. *Geology* **45**, 923–926 (2017).
37. Mitchell, N. C., Allerton, S. & Escartin, J. Sedimentation on young ocean floor at the Mid-Atlantic Ridge, 29°N. *Mar. Geol.* **148**, 1–8 (1998).
38. Ewing, J. & Ewing, M. Sediment distribution on the mid-ocean ridges with respect to spreading of the sea floor. *Science* **156**, 1590–1592 (1967).
39. Divins, D. L. Total sediment thickness of the world's oceans & marginal seas. NOAA National Geophysical Data Center (2003).
40. Johnson, H. P. & Pruis, M. J. Fluid and heat from the oceanic crustal reservoir. *Earth Planet. Sci. Lett.* **216**, 565–574 (2003).
41. Tucholke, B. W., Stewart, K. W. & Kleinrock, M. C. Long-term denudation of ocean crust in the central North Atlantic Ocean. *Geology* **25**, 171–174 (1997).
42. Cannat, M., Mangeny, A., Ondréas, H., Fouquet, Y. & Normand, A. High-resolution bathymetry reveals contrasting landslide activity shaping the walls of the Mid-Atlantic Ridge axial valley. *Geochem. Geophys. Geosyst.* **14**, 996–1011 (2013).
43. Olive, J.-A. & Escartin, J. Dependence of seismic coupling on normal fault style along the Northern Mid-Atlantic Ridge. *Geochem. Geophys. Geosyst.* **17**, 4128–4152 (2016).
44. Liu, Y. & Ric, J. R. Spontaneous and triggered aseismic deformation transients in a subduction fault model. *J. Geophys. Res.* **112**, B09404 (2007).
45. Mark, H. F., Behn, M. D., Olive, J.-A. & Liu, Y. Controls on mid-ocean ridge normal fault seismicity across spreading rates from rate-and-state friction models. *J. Geophys. Res.* **123**, 6719–6733 (2018).
46. Einarsson, P. & Brandsdóttir, B. Seismological evidence for lateral magma intrusion during the July 1978 deflation of the Krafla volcano in NE-Iceland. *J. Geophys. Res.* **47**, 160–165 (1980).
47. Keir, D. et al. Evidence for focused magmatic accretion at segment centers from lateral dike injections captured beneath the Red Sea rift in Afar. *Geology* **37**, 59–62 (2009).
48. Bohnenstiehl, D. R., Dziak, R. P., Tolstoy, M., Fox, C. & Fowler, M. Temporal and spatial history of the 1999–2000 Endeavour Segment seismic series, Juan de Fuca Ridge. *Geochem. Geophys. Geosyst.* **5**, Q09003 (2004).
49. Tolstoy, M., Bohnenstiehl, D. R., Edwards, M. & Kurras, G. Seismic character of volcanic activity at the ultraslow-spreading Gakkel Ridge. *Geology* **29**, 1139–1142 (2001).
50. Skolotnev, S. G. et al. Crustal accretion along the northern Mid Atlantic Ridge (52°–57°N): preliminary results from expedition V53 of R/V Akademik Sergey Vavilov. *Ofioliti* **48**, 13–30 (2023).

Publisher's note Springer Nature remains neutral with regard to jurisdictional claims in published maps and institutional affiliations.

Springer Nature or its licensor (e.g. a society or other partner) holds exclusive rights to this article under a publishing agreement with the author(s) or other rightsholder(s); author self-archiving of the accepted manuscript version of this article is solely governed by the terms of such publishing agreement and applicable law.

© The Author(s), under exclusive licence to Springer Nature Limited 2024

Methods

Earthquake locations and mechanisms

Earthquakes on the northern Mid-Atlantic Ridge are far from seismographic stations and event detection is therefore limited to moderate and larger earthquakes ($M > 4.0$). In this study, we rely primarily on hypocentres reported by the National Earthquake Information Center (NEIC; <https://www.usgs.gov/programs/earthquake-hazards/national-earthquake-information-center-neic>). The NEIC routinely reports hypocentres for earthquakes $M \geq 4.5$ in this area, but only rarely for events smaller than $M 4.2$. To complement the NEIC hypocentres, we make use of surface-wave detections and locations calculated using intermediate-period (35–150 s) surface waves recorded on the Global Seismographic Network (GSN) using a global grid search⁵¹. The threshold for the surface-wave detector is about 4.7, but occasionally an event of that size will be missed in the NEIC catalogue.

Uncertainties for earthquake locations based on teleseismic P-wave arrivals are typically 10–20 km (ref. 52). They can be even larger for surface-wave detections⁵¹, which gives rise to substantial scatter in earthquake epicentres. We relocate them using cross-correlations of their Rayleigh and Love waveforms, without correcting for specific surface-wave radiation patterns⁵³. This yields clearly defined bands of seismicity with relative location uncertainty smaller than 2 km, based on the misfit of the very large numbers of differential travel times (Supplementary Table 1). Empirical location estimates, based on inversions of subsets of the available data, are smaller than about 5 km for all but five of the earthquakes. Because the absolute location of the earthquakes is not well constrained, we shift their latitudes by 0.054° (about 6 km) to the west in a manner that positions the central band of seismicity over the neovolcanic axis, as identified from bathymetric maps of the 54° N segment (Fig. 1a).

We calculate focal mechanisms for these events with the centroid-moment tensor algorithm used in the Global CMT project^{35,54}. Long-period (>40 s) body-wave and surface-wave seismograms recorded on the GSN are matched to estimate the six elements of the moment tensor and an earthquake centroid location in time and space. We follow the procedure used in the standard Global CMT processing³⁵ and attempt analysis of all events with at least one reported magnitude of 4.7 or larger. The focal mechanisms for all earthquakes shown here are available in the Global CMT catalogue.

Between 26 September 2022 and 30 January 2023, 125 events yield stable and robust moment-tensor results, using the same quality criteria used in the standard Global CMT processing. Figure 1a shows the focal mechanisms of the 125 earthquakes plotted at their reported epicentres. Most of the events ($n = 113$) have normal-faulting geometries, with the remaining events ($n = 12$) having reverse mechanisms. The fault strikes of both normal and reverse mechanisms are generally north–south, with some variability. Fault dips also show variability. It is likely that much of the variation can be attributed to uncertainties in the moment-tensor estimates as many events are small ($M < 5$) and the dip-slip components of the moment tensor are difficult to constrain for shallow sources using long-period seismograms⁵⁵.

The 47 earthquakes shown in Fig. 1b occurred between 10 August 1990 and 14 June 2019 on the Carlsberg Ridge. These have been analysed previously as part of the Global CMT project. Here we relocated them using the surface-wave cross-correlation method described above, again yielding a clear central band of extensional events (Supplementary Table 1). All earthquake locations were shifted by 0.0581° (about 6 km) to the east and by 0.0436° (about 5 km) to the north to align the central band with the ridge axis.

Hypocentre depths for the 2022 Mid-Atlantic Ridge swarm

Hypocentre depths are not well constrained in standard location algorithms that mainly rely on first-arriving P waves. Uncertainties are typically on the order of 10 km. The long-period body and surface

waves used in the CMT analysis are similarly insensitive to the earthquake depth. To obtain better depth estimates, we examine the P-wave waveforms recorded at teleseismic distances. At these distances, the first-arriving P wave is followed by phases reflected off the surface of the Earth or off internal boundaries above the source. The delay times of the most prominent reflections pP and sP can sometimes be used to infer a depth when the duration of the source is shorter than the difference in the travel time of the two phases. For very shallow earthquakes, the reflected phases overlap the direct phase, creating a complicated waveform.

We examined P-wave waveforms for the $M 5.7$ normal-faulting earthquake on September 26 and the three largest reverse-faulting earthquakes on 29 September ($M 5.8$), 1 October ($M 5.9$) and 29 November 2022 ($M 5.5$). The waveforms show P-wave polarities consistent with the Global CMT focal mechanisms. When the pulses are filtered to reflect ground displacement, it becomes clear that, at many stations, the initial P-wave onset is followed nearly immediately (within 1–3 s) by an arrival of opposite polarity. We interpret this as interference by ocean-bottom and ocean-surface reflected phases. A delay of about a second between the P-wave onset and the change of displacement polarity observed at some stations is consistent with very shallow earthquake depth (<5 km). To obtain a more robust depth estimate, it is necessary to model the interference of the direct and reflected phases. We model the broadband teleseismic P wave using the method in ref. 56. In this technique, the broadband P-wave waveforms are synthesized in a layered elastic structure including a water layer. The depth, focal mechanism and moment-rate function are varied to obtain, in a least-squares sense, the best fit between observed and synthetic waveforms. The CMT solution is used as a soft constraint on the focal mechanisms to stabilize the inversion. We used a simple elastic model with an 8-km-thick oceanic crust overlain by an ocean layer. We estimated the water depth at the locations of each of the four earthquakes from the bathymetry. For the normal-faulting earthquake, we used a water depth of 2,000 m (bottom of the axial valley) and for the reverse-faulting earthquakes, we used depths between 1,200 and 1,500 m (top of the ridge flanks).

The results from the broadband P-wave inversions are consistent with the qualitative interpretation of the polarity change as resulting from early reflected phases. The best-fitting point-source focal depths below the ocean surface range between 2.7 and 4.2 km, corresponding to depths in the top 3 km in the crust. In the inversion, these depths are primarily constrained by the early part of the waveform and the observed early polarity change. Because the earthquake durations are longer than the delay between the direct and reflected phases, the depth of the full rupture may be larger than the estimated point-source depth. The inversion results constrain the initial part of the rupture to have occurred at very shallow depth in the crust (<3 km). The later part of the rupture may have extended deeper. A summary of our depth estimates is included in Supplementary Table 1.

Fault strain from bathymetric analyses

To estimate the fraction of plate separation T taken up by slip on large faults, we use a standard method to calculate the cumulative vertical displacement (throw) of faults^{22–24}. This method consists of identifying fault scarps in ridge-normal transects of high-resolution ship-board bathymetry and summing their vertical offsets as a function of along-profile distance. We specifically select steep, axis-facing slopes bounded by sharp breaks (Fig. 1c,d), to minimize confusion with volcanic features⁵⁷. Because of mass wasting and other seafloor-reworking processes^{41,42}, the vertical offset on a scarp is generally considered a more reliable estimator of vertical fault offset than its horizontal extent⁵⁸. We therefore use scarp throw as a proxy for fault throw and divide it by the tangent of the assumed fault dip to assess fault heave. Numerical models suggest that MOR faults rapidly rotate from their steep initial angles (> 50°) to shallower dips closer to 45° (ref. 59), consistent with the focal mechanisms in our catalogue. We therefore

assume a dip of 45° for all faults in this study. We then construct plots of the cumulative horizontal offset on faults as a function of distance to the axis (the position of the midpoint of each fault scarp). These typically show a linear trend with slope T close to the axis and a sharp decrease in slope ($T' < T$) \approx 15 km off-axis. It should be noted that assuming a dip of 45° only affects the absolute value of T , which can be straightforwardly adjusted to account for a different fault dip. We use a nonlinear least-squares method to fit a continuous, piecewise linear function with slopes T and T' before and after a cut-off distance x_c , with y intercept y_0 , to all our plots of cumulative offset versus distance. The only constraint enforced on T , T' and y_0 is that they are positive, whereas x_c must be greater than the distance of the first fault to the axis. Bathymetric data for the 54° N segment of the Mid-Atlantic Ridge is from ref. 50.

Candidate unfauling events across the global MOR system

We searched the Global CMT catalogue³⁵ for reverse-faulting events indicative of ridge-normal compression within about 50 km of a MOR axis²⁰. We retained those located in areas with sufficient shipboard bathymetric coverage—as compiled in the NCEI (NOAA) and GMRT (LDEO/NSF) repositories, and by further sources listed in the corresponding figure captions—to perform the fault strain analysis described in the previous section. These earthquakes are plotted in Fig. 4b and listed in Supplementary Table 2. They occurred in 13 sections of the Southwest Indian Ridge, Carlsberg Ridge, Mid-Atlantic Ridge and Southeast Indian Ridge, spanning ultraslow, slow and intermediate spreading rates. Corresponding maps are shown in Fig. 1 and Extended Data Figs. 1 and 3. Ten of these 13 sections feature regularly spaced abyssal hills bounded by steep, axis-facing normal faults and can be unambiguously classified as magmatically robust following the criteria of ref. 21. The other three (Extended Data Fig. 3d,e,h) feature corrugated surfaces typical of large-offset detachment faults, although the reverse-faulting earthquakes typically occurred beneath a terrain dissected by steep, closely spaced faults (within a typical location uncertainty of 10–20 km). This is evident from the bathymetric profiles we gathered in each location, which are plotted in Extended Data Figs. 4 and 5. The results of our strain analyses are compiled in Supplementary Table 3. All sections showed evidence for unfauling, with $T - T'$ averaging 0.09 ± 0.04 (Fig. 4c).

Lack of unfauling near an axial high: the East Pacific Rise at 9° 30' N

We performed one further strain analysis in a bathymetric profile across the fast-spreading East Pacific Rise at 9° 30' N (Extended Data Fig. 9). Of all the ridge sections we analysed, this is the only one in which the nonlinear least-squares fit yielded a value of T' (0.04) greater than T (0.01). This is consistent with the model of ref. 34, in which lithospheric unbending away from an axial high results in shallow extension. This configuration can be viewed as reciprocal to the shallow compression induced by unbending away from an axial valley, which drives unfauling (Fig. 3a). It further suggests that the decrease in apparent T fraction observed in all profiles that straddle ridge valley shoulders cannot be solely because of seafloor-reworking processes such as mass wasting or sedimentation. This is because these processes are probably active at the East Pacific Rise, at which the apparent T fraction increases away from the ridge axis.

Numerical modelling of MOR relief and stress

Using the approach in ref. 30, we conducted 2D numerical simulations of magmatic injection and fault growth at an idealized MOR with a fixed thermal structure. This approach builds on a series of spreading centre models^{7,27,29} that used FLAC (Fast Lagrangian Analysis of Continua), an explicit hybrid finite-element and finite-difference technique, to solve the equations of mass, momentum and energy conservation in a visco-elastic-plastic continuum. This method is well

suitable to simulating localized deformation, approximating faulting, and is described in detail elsewhere^{60–62}.

We consider deformation in a 2D model domain 150 km wide and 20 km deep (Fig. 3a). The top boundary is stress-free and the bottom boundary is a Winkler foundation, simulating flotation on an inviscid substrate with a mantle density. The sides are pulled at a constant velocity (full rate: $2U = 2.5 \text{ cm year}^{-1}$) and crustal material is added by means of dyking and lower crustal intrusion at the model centre, as described below. Regridding of the distorted Lagrangian mesh occurs regularly and returns the base and sides of the model domain to their original positions. Mantle material is added or subtracted at the base during regridding.

Both the crustal and mantle material are assigned a visco-elastic-plastic rheology with a viscosity that reflects a power law relating strain rate to the differential stress to the power $n = 3$ and an Arrhenius dependence on temperature. The parameter values are those of dry diabase⁶³, which ensures that the region cooler than about 600 °C (lithosphere) behaves essentially elasto-plastically. Brittle-plastic deformation is described by a Mohr–Coulomb failure criterion with a friction coefficient of 0.63 and initial cohesion of 25 MPa. When this yield criterion is met, the material weakens with strain beyond yield, leading to the localization of brittle deformation in model fault zones. Following previous work that simulated both bending-related and stretching-related faulting²⁷, we consider two phases of strain weakening. 10 MPa of cohesion loss occurs over 1% of plastic strain, followed by 13 MPa of further cohesion loss over 30% of strain. Our simulations do not account for the possibility of tensile failure. The model elements are 250 m wide and the fault zones in the model are typically about four elements wide⁶². The amount of fault slip necessary for total fault weakening (30% strain) is thus about 300 m. Both the crust and mantle are assigned a Young's modulus of 30 GPa and a Poisson's ratio of 0.25.

For simplicity, the thermal structure was fixed for the model shown in Fig. 3a, although similar models allowing self-consistent evolution of the thermal structure were used by ref. 31 to compare simulations with observed axial relief and faulting patterns as functions of spreading rate and crustal thickness. For the case shown in Fig. 3a, the seafloor was set to 20 °C and the depth of the 600 °C isotherm is set to 5 km at the ridge axis, which increases to 7 km at a distance of 40 km away from the axis. Temperature increases linearly with depth from the seafloor to the 600 °C isotherm. It also increases linearly between the 600 °C and 1,300 °C isotherms, but with five times the vertical temperature gradient. Temperature is capped at 1,300 °C throughout the deeper parts of the model.

Dyke intrusions accommodate the separation of plates at the spreading axis with a uniform average opening rate described by the M parameter (the fraction of plate spreading accommodated by dyking as defined by ref. 27), such that the dyke opening rate in the numerical model is defined as $2UM$. Instead of using a constant value for M , we follow the analysis of ref. 30 and relate it to crustal thickness (H_c) and on-axis lithosphere thickness (H_L) as follows:

$$M = \frac{H_c}{H_L + 0.5H_G} \quad (1)$$

In the above equation, H_c is the thickness of the magma column intruded into the asthenosphere resulting from the excess pressure associated with the development of the axial relief³⁰ and can be expressed as:

$$H_c = 0.25H_L + 0.5 \sqrt{\frac{9}{4}H_L^2 + \frac{6P_{DL}H_L}{(\rho_c - \rho_f)g}}, \quad (2)$$

in which ρ_c is the density of the crust, ρ_f is the density of the magma and P_{DL} is the driving pressure needed to open a metre-wide dyke. In the simulation shown in Fig. 3a, H_c is 7 km, ρ_c and ρ_f are set to $3,000 \text{ kg m}^{-3}$

and $2,700 \text{ kg m}^{-3}$, respectively, and P_{DI} is 10 MPa. We further prescribe minor oscillations in the amount of magma delivered to dykes, implemented as:

$$H_C(t) = H_C + \Delta M H_C \sin(2\pi\omega t). \quad (3)$$

In equation (3), ΔM and $1/\omega$ are the amplitude and period of the magma supply fluctuations, set to 0.15 and 0.2 Myr, respectively. $H_C(t)$ is then used in equation (1) to compute temporal fluctuations in M . These small fluctuations are set to enable the regular growth of normal faults that are evenly spaced by roughly 3 km.

Elastic stress changes caused by a dyke intrusion

We calculate the stress changes caused by 1 m of uniform opening on a vertical, 6 km tall by 50 km long rectangular dislocation embedded in an elastic half-space. The calculation is carried out with the MATLAB routines of ref. 64, which allow us to mesh the dyke with two triangular dislocations. The top of the dyke is set at 4 km below the surface. The Young's modulus and Poisson's ratio of the material are set to 10 GPa and 0.25, respectively⁶⁵. We compute the change in Coulomb failure stress⁶⁶ on 45°-dipping receiver faults striking parallel to the dyke, assuming a friction coefficient of 0.6. Wherever this stress change is positive, faults are brought closer to failure. We assess their favoured sense of slip by calculating their resolved shear stress, with the convention of negative shear stress indicating reverse motion. The results are shown in Fig. 3b. Because of the linearity of the problem, all stresses can be thought of as normalized by metre of opening on the axial dyke. We note that the compressive stress changes imparted by dyking across the ridge shoulders are approximately 100 times smaller than the absolute compressive stresses imparted by unbending (Fig. 3). Dyke-induced compression is thus not sufficient to reverse the sense of slip on abyssal-hill-bounding faults but could plausibly precipitate failure on faults already close to compressive yielding. Finally, it is important to note that the assumption of a homogeneous elastic half-space is warranted for rapid deformation events but probably overestimates stress changes, particularly if low-viscosity lower crust/asthenosphere can rapidly relax some of these stresses.

Data availability

All bathymetric data used in this study are from the published literature as referenced^{50,67,68} or openly available in the GMRT (<https://www.gmrt.org/>) and NOAA-NCEI (<https://www.ncei.noaa.gov/maps/bathymetry/>) repositories. The fault scarp dataset in ref. 24 is provided in Supplementary Table 4. Earthquake data are from the Global CMT catalogue (<https://www.globalcmt.org/CMTsearch.html>), except for earthquake relocations, which are provided in Supplementary Table 1.

Code availability

The simulation shown in Fig. 3a was run with the version of the FLAC code⁶⁰ developed in refs. 30,31. This code and the corresponding visualization scripts are available from the corresponding author on

reasonable request. The stress calculations shown in Fig. 3a were carried out with the code openly distributed with ref. 64.

51. Ekström, G. Global detection and location of seismic sources by using surface waves. *Bull. Seismol. Soc. Am.* **96**, 1201–1212 (2006).
52. Smith, G. P. & Ekström, G. Interpretation of earthquake epicenter and CMT centroid locations, in terms of rupture length and direction. *Phys. Earth Planet. Inter.* **102**, 123–132 (1997).
53. Howe, M., Ekström, G. & Nettles, M. Improving relative earthquake locations using surface-wave source corrections. *Geophys. J. Int.* **219**, 297–312 (2019).
54. Dziewowski, A. M., Chou, T.-A. & Woodhouse, J. H. Determination of earthquake source parameters from waveform data for studies of global and regional seismicity. *J. Geophys. Res.* **86**, 2825–2852 (1981).
55. Ekström, G. & Dziewowski, A. M. Centroid-moment tensor solutions for 35 earthquakes in Western North America (1977–1983). *Bull. Seismol. Soc. Am.* **75**, 23–39 (1985).
56. Ekström, G. A very broad band inversion method for the recovery of earthquake source parameters. *Tectonophysics* **166**, 73–100 (1989).
57. Escartin, J. & Olive, J.-A. in *Treatise on Geomorphology* 2nd edn 847–881 (Elsevier, 2022).
58. Hughes, A. et al. Quantification of gravitational mass wasting and controls on submarine scarp morphology along the Roseau fault, Lesser Antilles. *J. Geophys. Res. Earth Surface* **126**, e2020JF005892 (2021).
59. Olive, J.-A. & Behn, M. D. Rapid rotation of normal faults due to flexural stresses: an explanation for the global distribution of normal fault dips. *J. Geophys. Res.* **119**, 3722–3739 (2014).
60. Cundall, P. A. Numerical experiments on localization in frictional materials. *Ing. Arch.* **59**, 148–159 (1989).
61. Poliakov, A. N. B., Podladchikov, Y. & Talbot, C. Initiation of salt diapirs with frictional overburdens: numerical experiments. *Tectonophysics* **228**, 199–210 (1993).
62. Lavier, L. L., Buck, W. R. & Poliakov, A. N. B. Factors controlling normal fault offset in an ideal brittle layer. *J. Geophys. Res.* **105**, 23431–23442 (2000).
63. Mackwell, S. J., Zimmerman, M. E. & Kohlstedt, D. L. High-temperature deformation of dry diabase with application to tectonics on Venus. *J. Geophys. Res.* **103**, 975–984 (1998).
64. Meade, B. J. Algorithms for the calculation of exact displacements, strains, and stresses for triangular dislocation elements in a uniform elastic half space. *Comput. Geosci.* **33**, 1064–1075 (2007).
65. Heap, M. J. et al. Towards more realistic values of elastic moduli for volcano modelling. *J. Volcanol. Geotherm. Res.* **390**, 106684 (2020).
66. King, G. C. P., Stein, R. S. & Lin, J. Static stress changes and the triggering of earthquakes. *Bull. Seismol. Soc. Am.* **84**, 935–953 (1994).
67. Maia, M. COLMEIA cruise. RV L'Atalante. <https://doi.org/10.17600/13010010> (2013).
68. Maia, M. et al. Extreme mantle uplift and exhumation along a transpressive transform fault. *Nat. Geosci.* **9**, 619–623 (2016).

Acknowledgements G.E. received support from the Consortium for Monitoring, Technology, and Verification under the Department of Energy National Nuclear Security Administration award number DE-NA0003920. Z.L. was supported by the JLU Science and Technology Innovative Research Team programme (no. 2021TD-05). M.B. was supported by the ISblue project (Interdisciplinary Graduate School for the Blue Planet: ANR-17-EURE-0015) co-funded by a France 2030/Investissement d'Avenir grant from the French government. We thank our editor and the reviewers for their insightful feedback. We also thank I. Grevemeyer, S. Cesca, S. Solomon and A. Janin for helpful discussions. J. Chen and L. C. Malatesta provided valuable assistance with figure design. Finally, we thank S. Skolotnev and M. Ligi for providing the Mid-Atlantic Ridge 54°N bathymetric data.

Author contributions J.-A.O. designed the study, conducted the bathymetric analyses with J.E. and M.B., carried out the elastic stress modelling and wrote the initial manuscript. G.E. compiled and analysed the earthquake data. W.R.B. and Z.L. designed the models of ridge flank flexure. All authors discussed and analysed the results and provided feedback on the manuscript.

Competing interests The authors declare no competing interests.

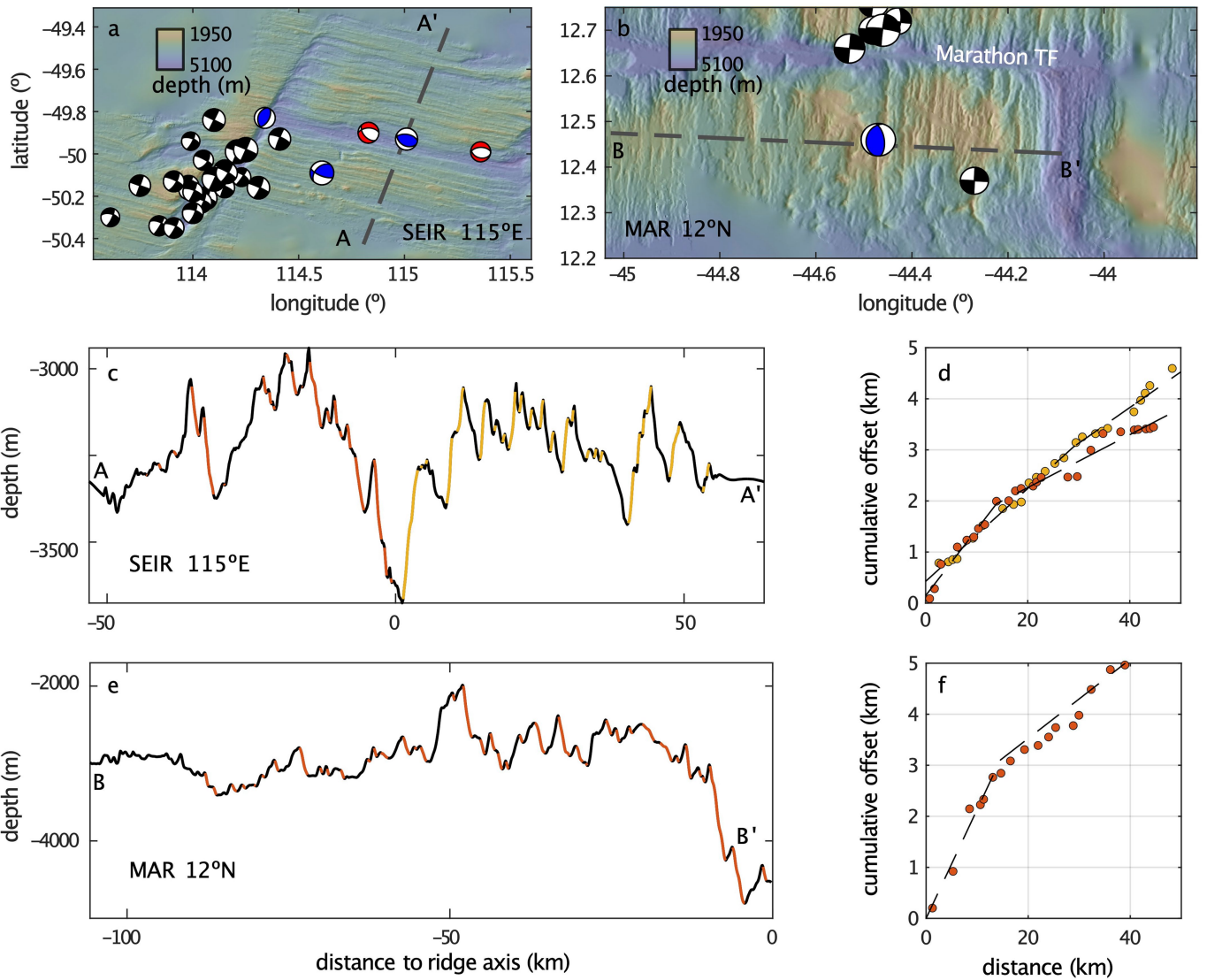
Additional information

Supplementary information The online version contains supplementary material available at <https://doi.org/10.1038/s41586-024-07247-w>.

Correspondence and requests for materials should be addressed to Jean-Arthur Olive.

Peer review information *Nature* thanks Delwayne Bohnstiehl, Ingo Grevemeyer and the other, anonymous, reviewer(s) for their contribution to the peer review of this work.

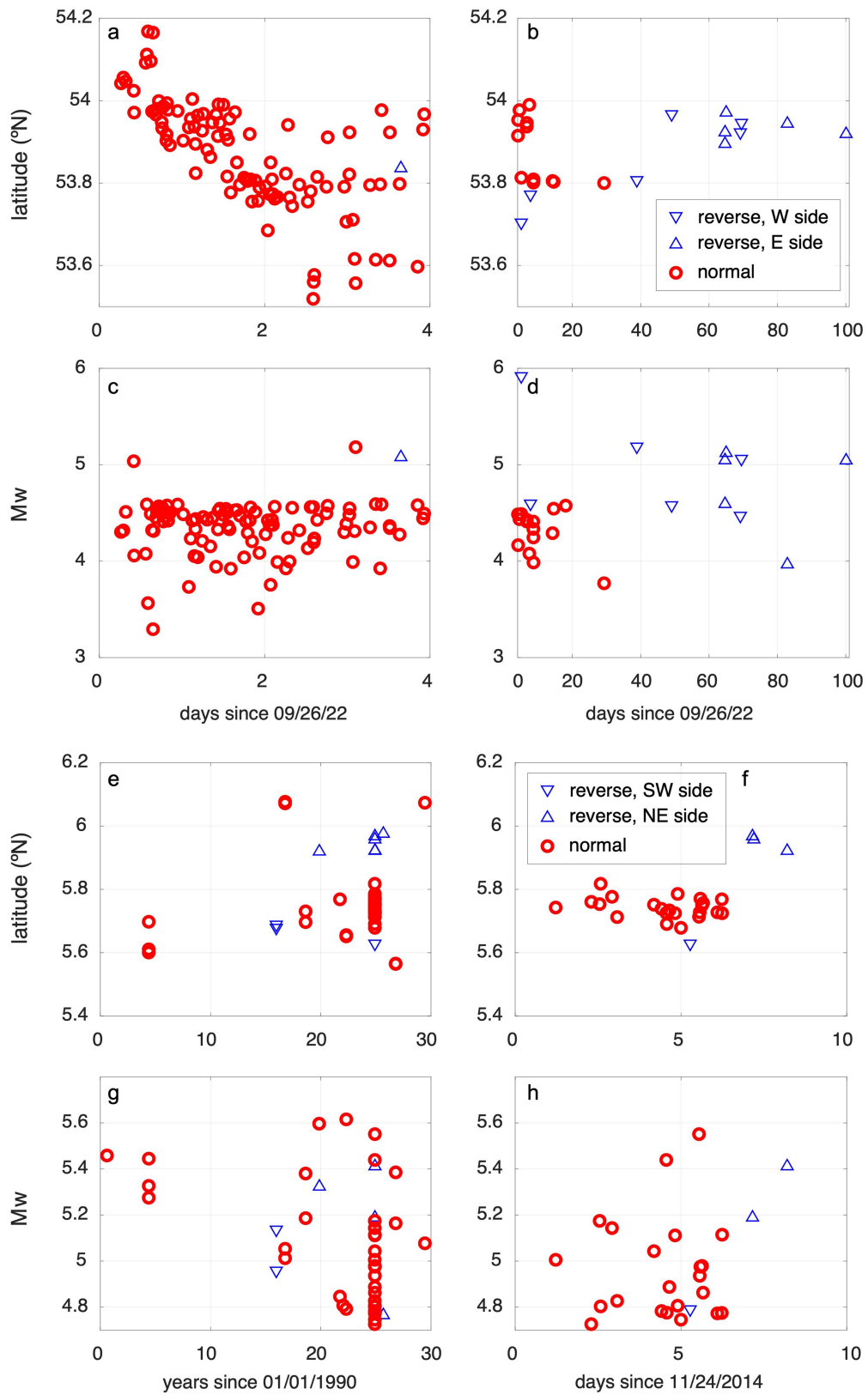
Reprints and permissions information is available at <http://www.nature.com/reprints>.



Extended Data Fig. 1 | Examples of near-axis compression at MORs.

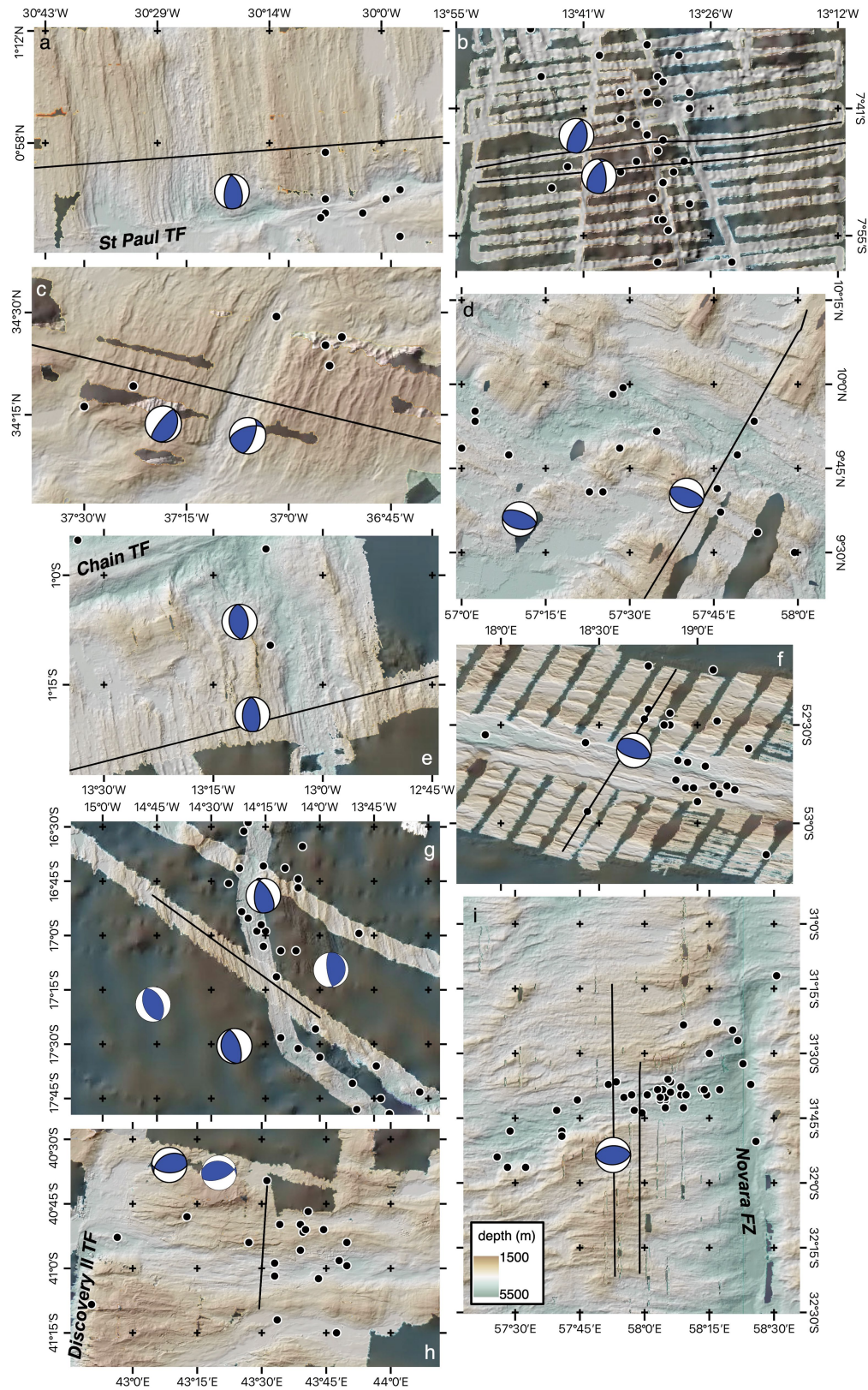
a, Bathymetric map of the Southeast Indian Ridge (SEIR) near 115° E, with focal mechanisms from the CMT catalogue. **b**, Bathymetric map of the Mid-Atlantic Ridge (MAR) south of the Marathon transform fault (TF), with focal mechanisms from the CMT catalogue. **c**, Bathymetric profile across the SEIR (dashed line in panel **a**), with coloured segments indicating fault scarps. **d**, Cumulative fault heave versus distance from the axis for the southern (red) and northern (yellow)

sides of the SEIR, with best-fitting piecewise linear functions shown as dashed lines ($T = 0.13$, $T' = 0.05$ on the south side; $T = 0.09$, $T' = 0.07$ on the north side). **e**, Bathymetric profile across the western flank of the MAR (dashed line in panel **b**), with coloured segments indicating fault scarps. **f**, Cumulative fault heave versus distance from the axis for the western side of the MAR, with best-fitting piecewise linear function shown as dashed lines ($T = 0.21$, $T' = 0.08$).



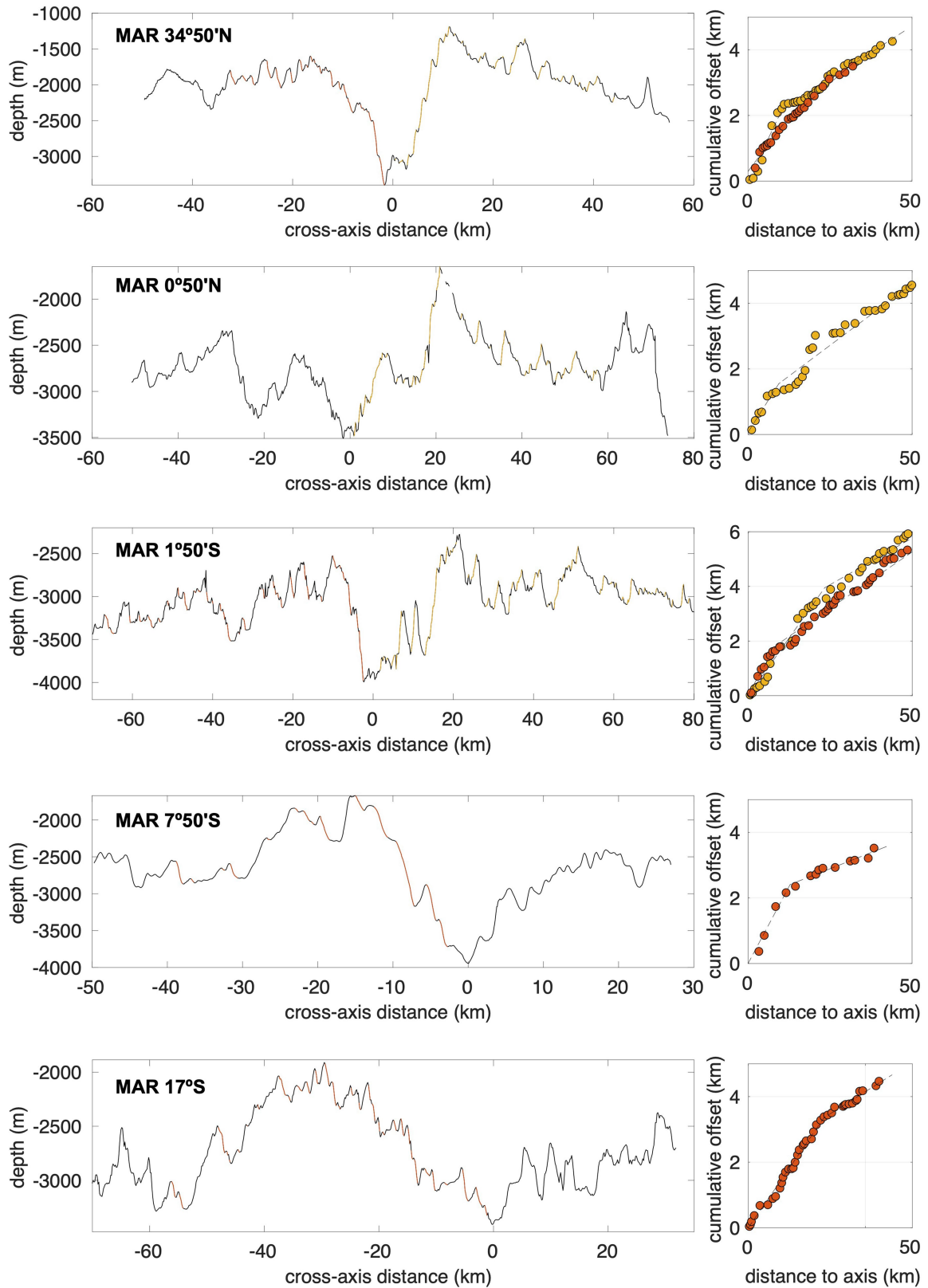
Extended Data Fig. 2 | The 2022 northern Mid-Atlantic Ridge and 2014 Carlsberg Ridge seismic sequences. Latitude and moment magnitude of earthquakes, colour-coded by mechanism (blue, reverse faulting; red, normal

faulting) and location, throughout the 2022 Mid-Atlantic Ridge sequence (a–d) and 2014 Carlsberg Ridge sequence (e–h).



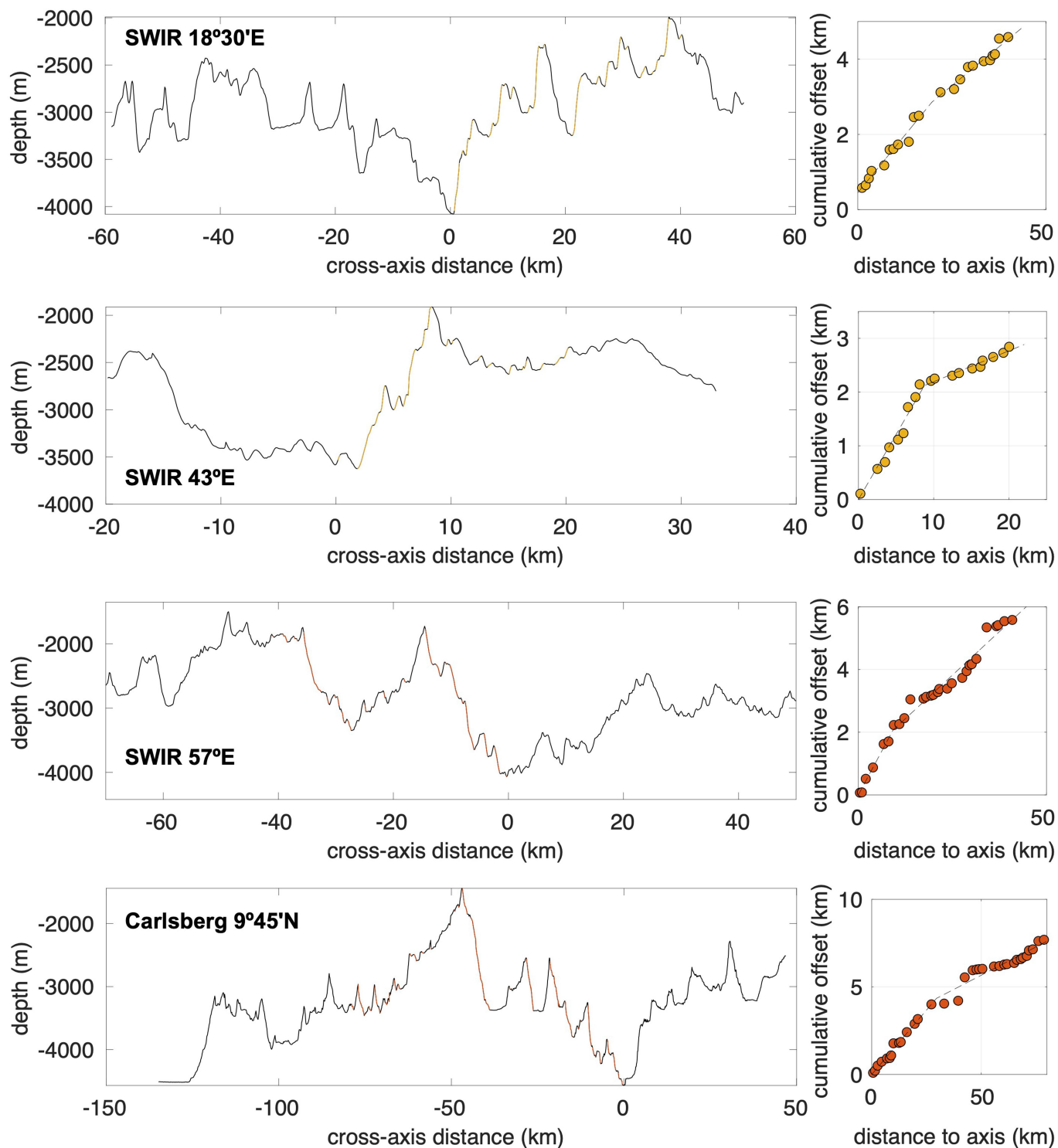
Extended Data Fig. 3 | Examples of near-axis reverse-faulting earthquakes at MORs. Bathymetric maps, reverse focal mechanism and profile used for strain analyses at the Mid-Atlantic Ridge 0° 50' N near the St. Paul transform fault (TF)^{67,68} (a); Mid-Atlantic Ridge 7° 50' S (b); Mid-Atlantic Ridge 34° 50' N (c);

Carlsberg Ridge 9° 45' N (d); Mid-Atlantic Ridge 1° 20' S (e); Southwest Indian Ridge 18° 30' E (f); Mid-Atlantic Ridge 17° S (g); Southwest Indian Ridge 43° E near the Discovery II transform fault (TF) (h); and Southwest Indian Ridge 57° E (i). FZ, fracture zone.



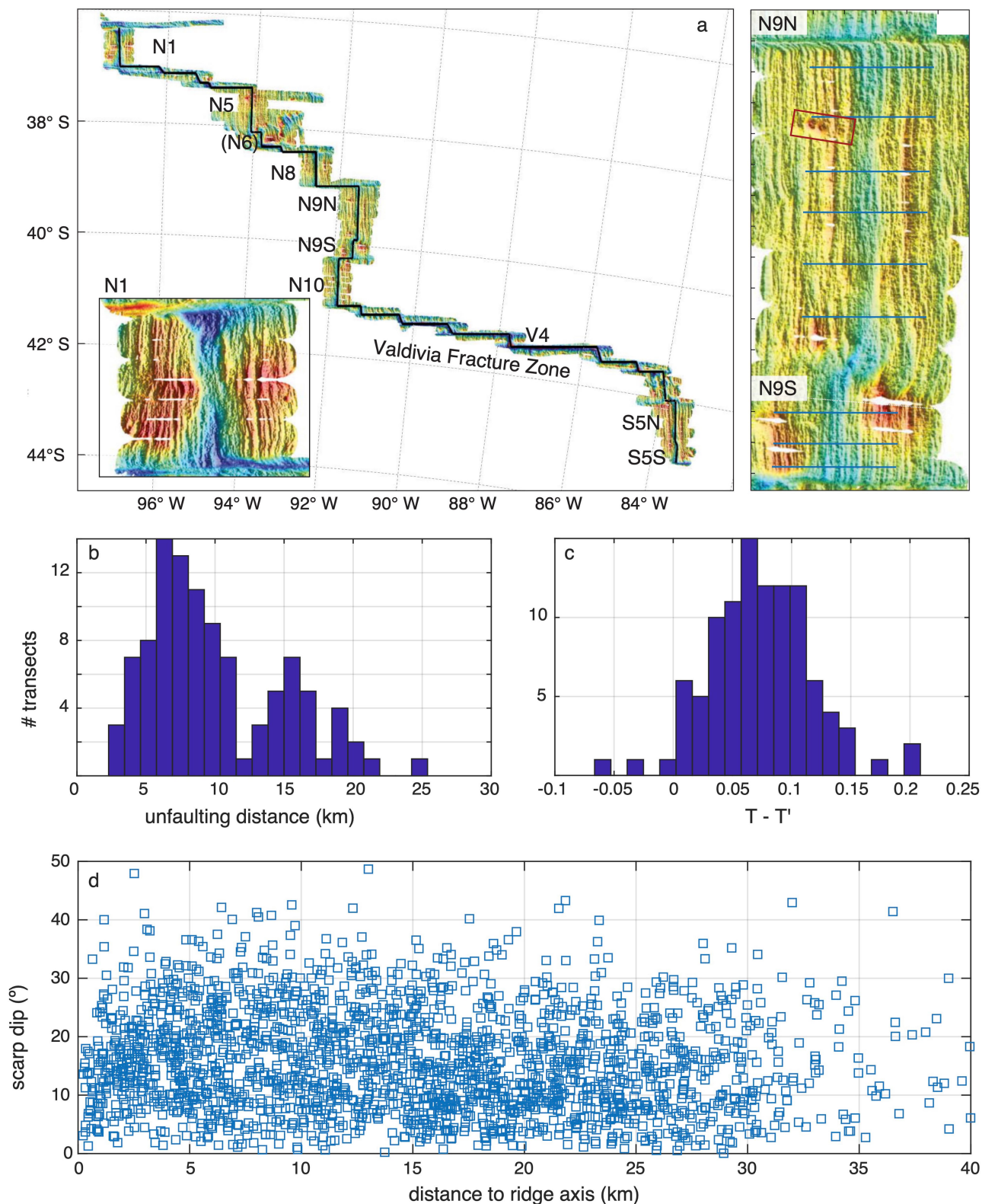
Extended Data Fig. 4 | Bathymetric signatures of unfaulting in the Atlantic Ocean. Left, bathymetric cross-sections with fault scarps highlighted in colour. Right, plots of cumulative fault heave versus distance at selected

sections of the Mid-Atlantic Ridge. Corresponding values of T , T' and x_c are listed in Supplementary Table 3.



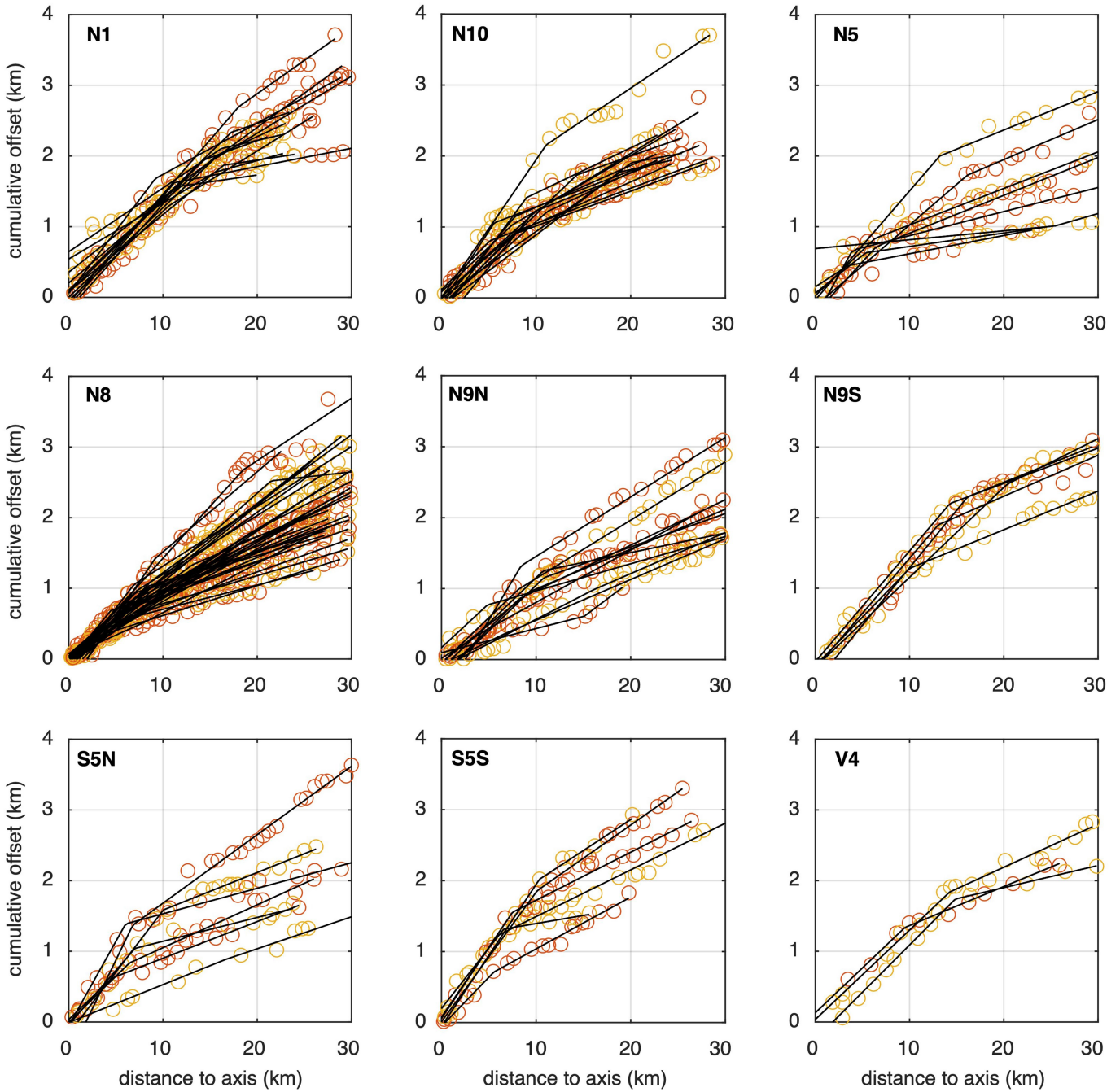
Extended Data Fig. 5 | Bathymetric signatures of unfaulting in the Indian Ocean. Left, bathymetric cross-sections with fault scarps highlighted in colour. Right, plots of cumulative fault heave versus distance at selected

sections of the Southwest Indian Ridge and the Carlsberg Ridge. Corresponding values of T , T' and x_c are listed in Supplementary Table 3.



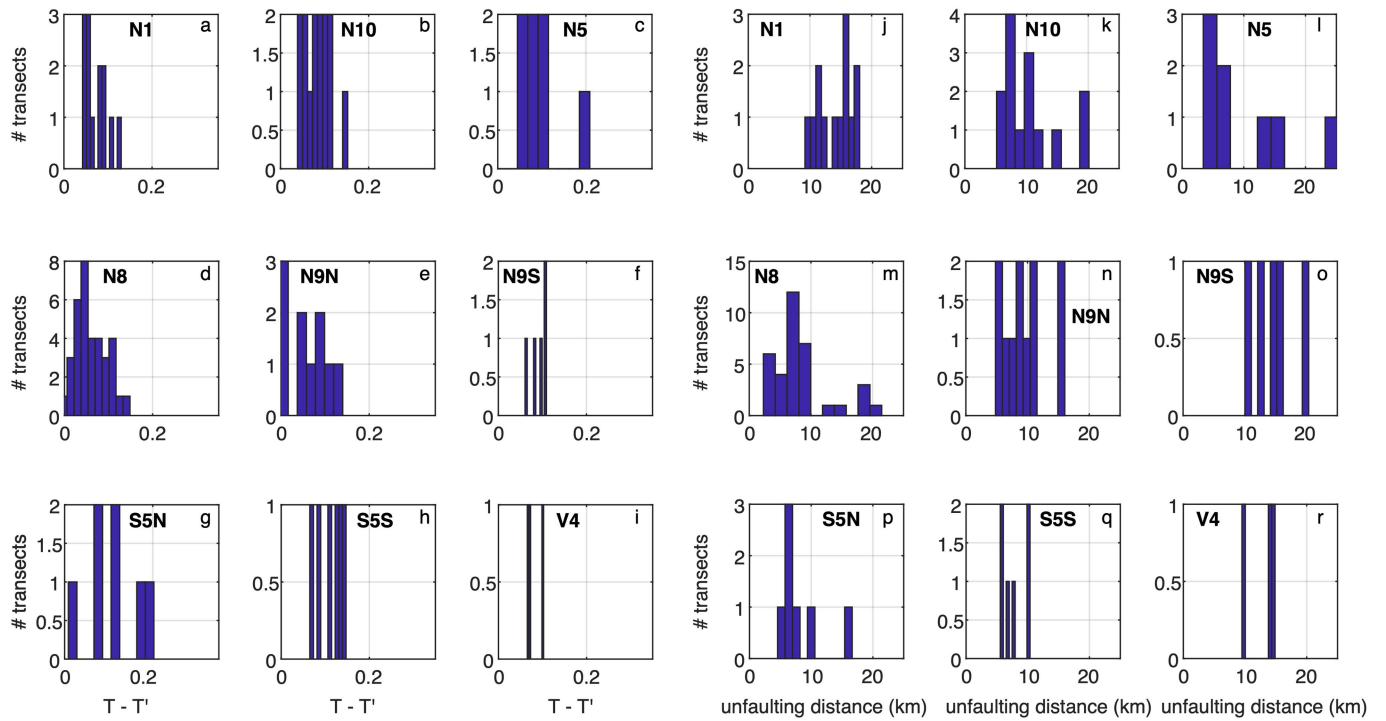
Extended Data Fig. 6 | Unfaulting along the intermediate-spreading Chile Ridge. **a**, Bathymetric map of the Chile Ridge axis outlining its main segments, adapted from ref. 24. Insets detail bathymetry of segments N1 and N9N–N9S. Position **(b)** and amplitude **(c)** of the change in apparent T at the Chile Ridge:

histograms of x_c and $(T - T')$ for all transects across the Chile Ridge, excluding poor fits highlighted in grey in Supplementary Table 3. **d**, Average slope of axis-facing scarps versus distance to the ridge axis. Data are from the fault scarp compilation of ref. 24.



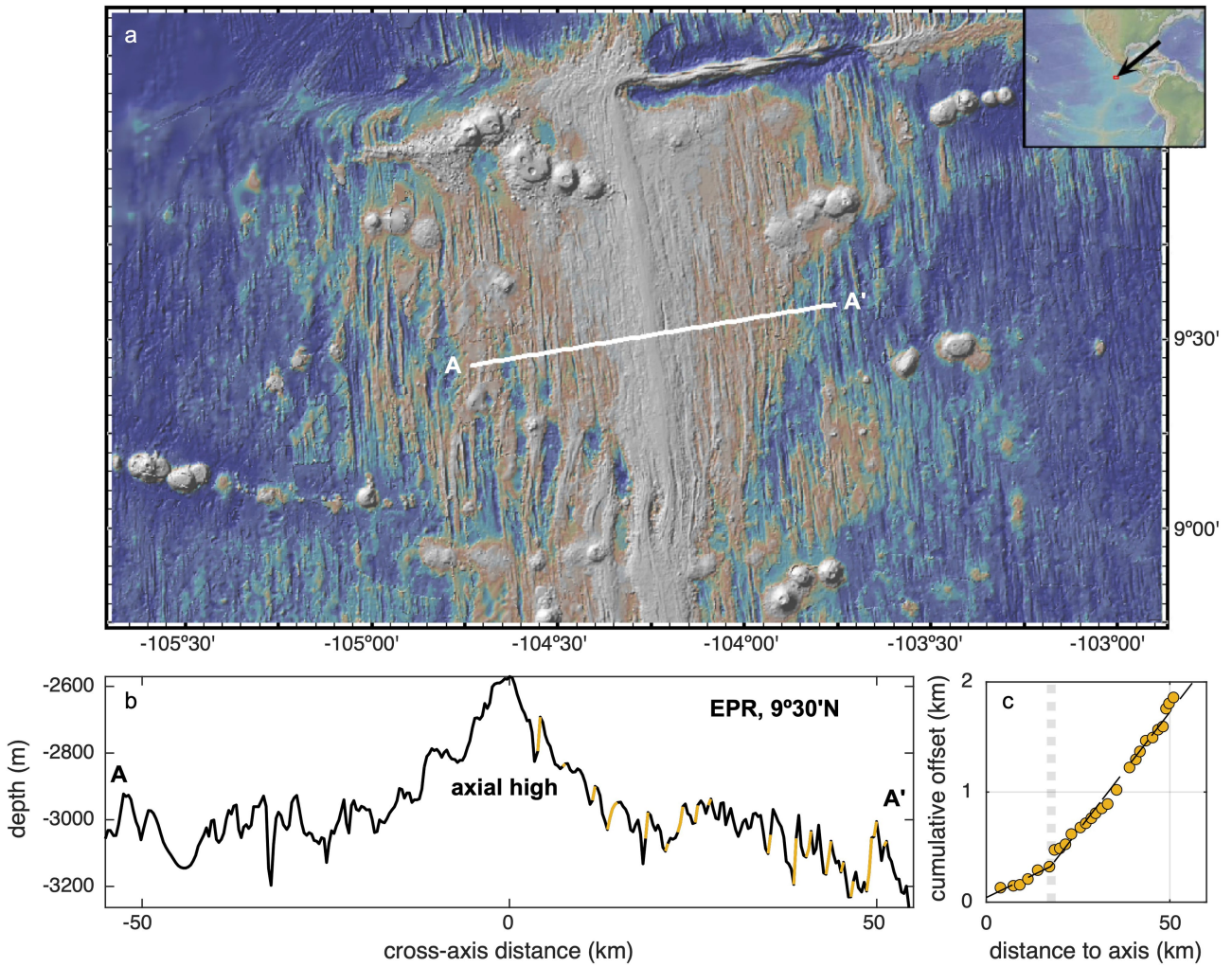
Extended Data Fig. 7 | Tectonically accommodated strain along the Chile Ridge. Cumulative fault heave versus distance from the axis along individual transects from each segment of the Chile Ridge, based on the fault scarp compilation of ref. 24. Red and yellow dots correspond to the western and

eastern sides of the axis, respectively, with best-fitting piecewise linear functions shown as black lines. This excludes poor fits highlighted in grey in Supplementary Table 3.



Extended Data Fig. 8 | Amplitude and position of the change in apparent T along the Chile Ridge. a-i, Histograms of the amplitude of the change ($T - T'$) in apparent T in each bathymetric transect, grouped by segment. **j-r,** Histograms

of the distance x_c for which the change in apparent T occurs in each bathymetric transect. These plots exclude poor fits highlighted in grey in Supplementary Table 3.

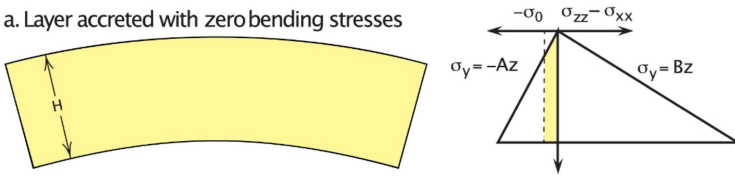


Extended Data Fig. 9 | Lack of unfaulting near an axial high. **a**, Bathymetric map of the fast-spreading East Pacific Rise at 9° 30' N, which—unlike every other ridge section studied here—features an axial high instead of an axial valley. White line indicates the location of the bathymetric transect. **b**, Bathymetric

cross-sections with fault scarps highlighted in colour. **c**, Cumulative fault heave versus distance, with best-fitting piecewise linear function shown as black lines. In this case, $T' > T$.

Article

a. Layer accreted with zero bending stresses



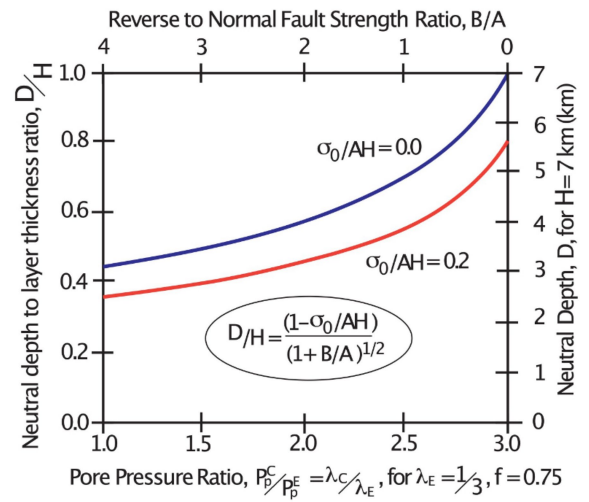
b. Flattened layer with strong reverse faults



c. Flattened layer with weak reverse faults



d. Depth extent of ridge shoulder compression



Extended Data Fig. 10 | Mechanics of ridge shoulder unbending. The yield stress of the lithosphere σ_y is defined as the difference between the vertical and horizontal stresses needed to produce fault slip. **a.** An idealized plate that was accreted with curvature and no bending stresses. σ_0 is an assumed background stress difference. The simple case shown has no cohesion and parameters A and B depend strongly on the friction coefficient f and assumed pore pressure P_p on the faults, as defined in the Supplementary Information. **b.** A case with reverse faults that are three times stronger than normal faults. **c.** Deepening of the neutral depth, D , when the reverse faults are assumed to be weaker than the normal faults. **d.** Analytical estimate of the neutral depth D , which marks the

base of the compressive zone in an unbending ridge shoulder. The ratio of D to the layer thickness, H , is plotted versus the ratio of pore pressures on reverse versus normal faults assuming $f = 0.75$ and that the pore pressure on normal faults is one-third the lithostatic pressure (blue curve). Assuming a rock density of $3,000 \text{ kg m}^{-3}$ and water density of $1,000 \text{ kg m}^{-3}$, the left limit is for hydrostatic pore pressure on the reverse faults, whereas the right limit is for lithostatic pore pressure on the reverse faults. Red curve shows the effect on the neutral depth of a regional horizontal extensional stress difference equal to 20% of the extensional yield stress at the base of the layer. See Supplementary Information for details.